Lagrangian acceleration statistics in a turbulent channel flow

Nickolas Stelzenmuller,[1] Juan Ignacio Polanco,[2] Laure Vignal,[1]
Ivana Vinkovic,[2] and Nicolas Mordant[1,*]

[1]*Laboratoire des Ecoulements Géophysiques et Industriels, Université Grenoble Alpes & CNRS,*
Domaine Universitaire, CS 40700, F-38058 Grenoble, France
[2]*Laboratoire de Mécanique des Fluides et d'Acoustique, UMR 5509, Ecole Centrale de Lyon, CNRS,*
Université Claude Bernard Lyon 1, INSA Lyon, 36 av. Guy de Collongue, F-69134 Ecully, France

Lagrangian acceleration statistics in a fully developed turbulent channel flow at $\mathrm{Re}_\tau = 1440$ are investigated, based on tracer particle tracking in experiments and direct numerical simulations. The evolution with wall distance of the Lagrangian velocity and acceleration time scales is analyzed. Dependency between acceleration components in the near-wall region is described using cross-correlations and joint probability density functions. The strong streamwise coherent vortices typical of wall-bounded turbulent flows are shown to have a significant impact on the dynamics. This results in a strong anisotropy at small scales in the near-wall region that remains present in most of the channel. Such statistical properties may be used as constraints in building advanced Lagrangian stochastic models to predict the dispersion and mixing of chemical components for combustion or environmental studies.

I. INTRODUCTION

The Lagrangian study of fluid particle trajectories is a natural first step in predicting the transport of components that are passively entrained by the flow such as chemical and radioactive pollution (passive scalars), aerosols (with small inertia), or the mixing of components prior to combustion. Indeed, in many cases the Péclet number is very large so that most of the statistical properties of scalar dispersion are directly related to that of the dispersion of fluid particles (except of course at the smallest scales at which molecular diffusion plays an ultimate role that depends on the Schmidt number). Despite advances in computational power and resources, direct numerical simulations (DNS) are still out of reach in practical situations. Thus, an efficient modeling is required to obtain reliable predictions. Due to the random nature of turbulence, it is tempting to develop stochastic models that could be used for simulations with an average or large-scale knowledge of the flow. A growingly popular method is large eddy simulation (LES) in which only the largest scales of the turbulence are resolved whereas the small scales of the turbulent spectra are modeled [1]. Various classes of models can be used for the unresolved part of the flow, and Lagrangian stochastic subgrid models can be developed for such simulations as used in combustion, for instance [2,3]. An efficient model would also be useful to forecast the dispersion of pollution from localized sources (e.g., industrial accident) using coarse-grid meteorological predictions.

In the context of homogeneous and isotropic turbulence (HIT), one-dimensional (1D) Lagrangian stochastic models have been developed as variations of the Langevin equation, i.e., modeling the velocity v of a fluid particle as a Markovian process [4]:

$$dv = -\frac{v}{T_L}dt + \left(\frac{2\sigma^2}{T_L}\right)^{1/2}dW(t) \tag{1}$$

---

*nicolas.mordant@univ-grenoble-alpes.fr

with T_L the Lagrangian integral time scale, $W(t)$ a Wiener process, and σ^2 the velocity variance. Due to the absence of correlations between velocity components this equation is 1D. It is so strongly constrained by symmetries and the input from the Kolmogorov 1941 theory that it involves only one parameter, $T_L = \frac{2\sigma^2}{C_0\epsilon}$ (with ϵ the average turbulent energy dissipation rate per unit mass and C_0 a universal constant). This approach incorporates naturally Taylor's classic result [5] of long-term turbulent diffusion of a single particle. This equation includes neither the dependency on the Reynolds number nor intermittency. Concerning the former point, this simple framework [Eq. (1)] has been extended by Sawford [6] to include finite Reynolds number effects. The model is now a second order stochastic equation that models the acceleration and no longer the velocity:

$$da = -\alpha_1 a\, dt - \alpha_2 \int_0^t a(s)\, ds\, dt + \sqrt{2\alpha_1\alpha_2\sigma^2}\, dW(t). \qquad (2)$$

Parameters α_1 and α_2 are two inverse time scales related to the Kolmogorov time scale $\tau_\eta = \sqrt{\nu/\epsilon}$ and the integral Lagrangian time scale T_L. The Reynolds number thus appears as the ratio of the two time scales. At very high Reynolds number, the Kolmogorov theory predicts that the ratio $\frac{T_L}{\tau_\eta} = \frac{2\mathrm{Re}_\lambda}{C_0\sqrt{15}}$ (with Re_λ the usual Taylor-scale Reynolds number). Sawford [6] suggested an empirical formula estimated from DNS at moderate Re_λ given by

$$\frac{T_L}{\tau_\eta} = \frac{2\mathrm{Re}_\lambda}{C_0\sqrt{15}}\big(1 + 7.5C_0^2\mathrm{Re}_\lambda^{-1.64}\big). \qquad (3)$$

This model remains Gaussian at all scales and thus does not include any intermittency effect. Moreover, it remains unidimensional with no interdependency between acceleration (or velocity) components. Real flows as encountered in nature (atmospheric boundary layer) or in industrial applications (pipes, mixers, combustion chambers, etc.) can rarely be considered as homogeneous and isotropic, notably due to nonzero average shear and wall confinement. Pope [7] showed that a homogeneous, anisotropic Langevin-type stochastic model should include the time scales associated with the auto- and cross-correlations of the acceleration and velocity components.

The last 20 years have seen the development of experimental techniques and DNS capabilities that have allowed the direct simultaneous observation of the acceleration, velocity, and position of fluid particles, mostly focused on HIT. They showed that acceleration statistics are strongly non-Gaussian (intermittent) [8]. Modeling such features requires us to further increase the dimensionality of the stochastic models in the framework of the nonextensive statistical mechanics [9–11] or to use a non-Markovian model [12]. In both cases, inspired by the Kolmogorov-Obukhov theory, dissipation which appears in the magnitude of the noise in the stochastic equations) is assumed to be itself a stochastic variable and fluctuates with a long time scale comparable to T_L. Thus, the stochastic equations involve multiplicative noise that make their developments much more involved.

Data concerning more realistic flows are scarce [13–19]. Complex models of inhomogeneous and anisotropic turbulence are weakly constrained by symmetries or scaling considerations and thus require significant experimental or numerical input. Del Castello and Clercx [16] studied anisotropic turbulence affected by rotation which remains quite far from realistic flows. Walpot *et al.* reported some Lagrangian statistics of velocity in the circular pipe flow and their incorporation in stochastic modeling but no acceleration data [15]. Gerashenko *et al.* [17] studied the case of inertial (heavy) particles in a boundary layer but not the case of the Lagrangian tracers. Chen *et al.* [14] provided Eulerian information on the acceleration in a turbulent channel flow but did not discuss the Lagrangian dynamics. Choi *et al.* [13] report a numerical analysis of the Lagrangian dynamics of acceleration in a turbulent channel flow, but their Reynolds number is relatively low, and they discuss neither the coupling between acceleration components nor the time scales. This article reports small-scale–resolved Lagrangian experimental measurements in a statistically stationary, high-aspect-ratio turbulent channel flow, as well as DNS results with parameters matching those of the experiment. Such a flow represents a relatively simple academic framework that incorporates the basic ingredients of real flows: average shear (anisotropy) and confinement (inhomogeneity). In
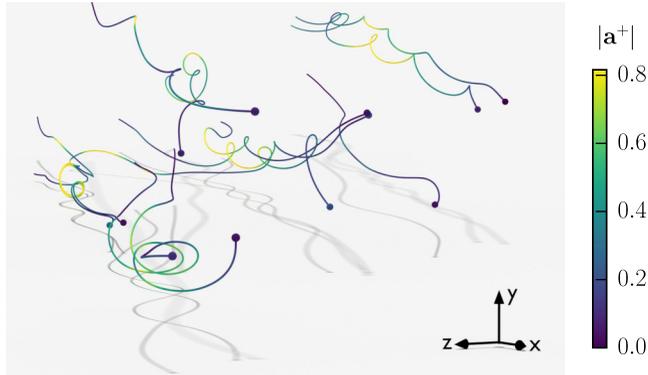
FIG. 1. Sample high-acceleration particle tracks obtained from DNS. Particles are located in the near-wall region ($y^+ \lesssim 200$). Trajectories are shown over $\Delta t^+ = 120$. The shadow is projected on the wall. Colors represent the norm of particle acceleration. $|\mathbf{a}^+| = 1$ corresponds roughly to $430 \, \text{m/s}^2$ in the experiments.

the fully developed part of the flow, the Eulerian statistics of the turbulence are stationary in time and translation-invariant in the streamwise and transverse direction. Because of these symmetries, the statistics can be conditioned on a single parameter, the wall distance y. This relative simplicity makes this flow a privileged framework to develop and benchmark advanced Lagrangian stochastic models applicable to realistic flows.

It is well known that near-wall turbulence is characterized by multiscale coherent structures with preferential orientations [20]. These structures include intense vortices elongated in the mean flow direction that strongly affect the near-wall flow dynamics. These streamwise vortices induce strong centripetal accelerations, being the main source of acceleration intermittency near the walls [21], as illustrated in Fig. 1. On the other hand, large-scale inhomogeneity implies that velocity and acceleration statistics depend on wall distance. Thus, it is also of interest to investigate the far-wall behavior, where a return to isotropy may be expected, and stochastic models based on isotropic turbulence may be applied.

We first present the experimental and numerical setups that allow us to measure the acceleration of particles along their trajectories. In Sec. III we show the statistical analysis of the temporal dynamics through the computation of time correlation functions of both acceleration and velocity components. This analysis provides estimates of the relevant time scales that are discussed in Sec. IV. In Sec. V we focus on the acceleration probability distributions and compare them to the case of HIT.

II. EXPERIMENTAL AND NUMERICAL SETUPS

We study the turbulent flow in a channel between two parallel walls separated by a distance $2h$ using the same Reynolds number ($\text{Re} = U_0 h / \nu = 34\,000$) in both experiments and DNS. This corresponds to a friction Reynolds number $\text{Re}_\tau = u_\tau h / \nu \approx 1440$, where $u_\tau = \sqrt{\tau_w / \rho}$ is the friction velocity associated to the shear stress τ_w at the wall and ν the kinematic viscosity. In the following, the superscript + indicates quantities expressed in wall units, nondimensionalized by u_τ and ν.

The experiment consists of measurements made in a closed-loop water tunnel, shown in Fig. 2, with a centerline velocity $U_0 = 1.75 \, \text{m/s}$. We chose water as a working fluid in order to have neutrally buoyant and small enough tracer particles, which is very difficult to achieve in air. The experimental test section is 3.2 m long with a cross section of $37.5 \times 316 \, \text{mm}$, with tripped boundary layers at the entrance. The development length is $155h$ and the channel height is $16.9h$, ensuring statistical homogeneity in the streamwise and spanwise directions.

The wall unit is $\delta = \nu / u_\tau = 13 \, \mu\text{m}$ in our experimental conditions; thus we chose to seed the flow with $10 \, \mu\text{m}$ polystyrene spheres that are small enough to accurately trace the flow down to
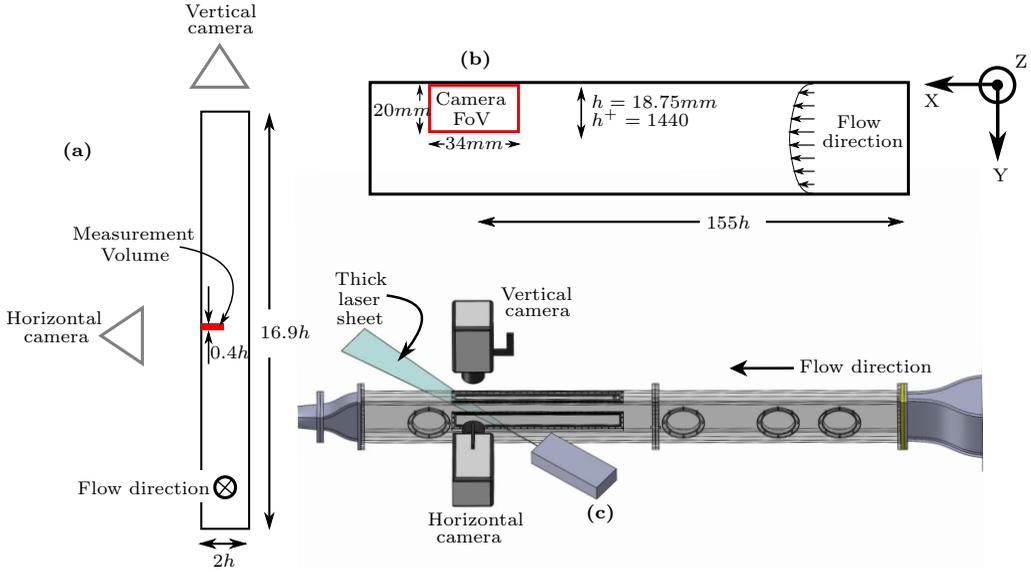
FIG. 2. Sketch of the turbulent channel used in the experiment. (a) A sketch of the end view of the channel showing the aspect ratio of the channel (the spanwise distance is 16.9*h*) and the end view of the measurement volume, as well as the position of the two cameras. (b) A top view of the channel, with the field of view (FoV) of the vertical camera highlighted. (c) A 3D rendering of the experimental setup, including the relative positions of the two high-speed cameras and the thick laser sheet used to illuminate the measurement volume.

the viscous layer. The Stokes number of these particles ranges from St $= 0.02$ at $y^+ = 0.5$ to St $= 9 \times 10^{-4}$ at the center of the channel. Fluorescent particles are used in order to improve the contrast in the vicinity of the wall by eliminating reflections of the illumination laser near the wall. This choice makes the measurement conditions quite challenging due to the weak amount of light emitted by the particles. Three-dimensional particle trajectories are measured by particle-tracking velocimetry [22] in a $35 \times 20 \times 8$ mm measurement volume illuminated by an 8 mm-thick 25W CW laser sheet, using two highly sensitive very high-speed Phantom v2511 cameras running at a sampling rate of 25 000 frames/s (with one 180 mm and one 150 mm macro lenses with optical filters tuned to the emission frequency of the fluorescent particles). The measurement volume covers half the width of the channel and is long enough in the downstream direction for a sufficiently long time of particle tracking. This allows us to observe the full decorrelation of the acceleration and (close to the wall) the velocity. Such a high sampling rate is required in order to have enough time resolution to differentiate twice the trajectories and compute the acceleration. Particle velocity and acceleration are obtained by convolution of the trajectories with Gaussian differentiating kernels, which also serves to filter out noise from the measurements [23]. The pixel size corresponds to 27 μm in physical space, but because of the diffraction of their emitted light, the fluorescent particles cover about three pixels in the images, which has been shown to be a good condition for subpixel position accuracy. Indeed, the estimated accuracy is 1/10th of a pixel (i.e., 3 μm) after filtering. Although this allows us to have a fairly precise estimation of the position of the particles in the bulk of the flow, the apparent size of the particle and the existence of images reflected in the wall prevents us from measuring the position of the particles very near the wall. The closest distance at which accurate detection of the particle was possible is $y^+ = 4$, i.e., about 50 μm. Thus, our range of measurement spans the interval $y^+ \in [4, 1400]$ i.e., more than two orders of magnitude in wall distance.

Direct numerical simulations are performed using a pseudospectral method for the resolution of the velocity field between two parallel walls, coupled with Lagrangian tracking of passive
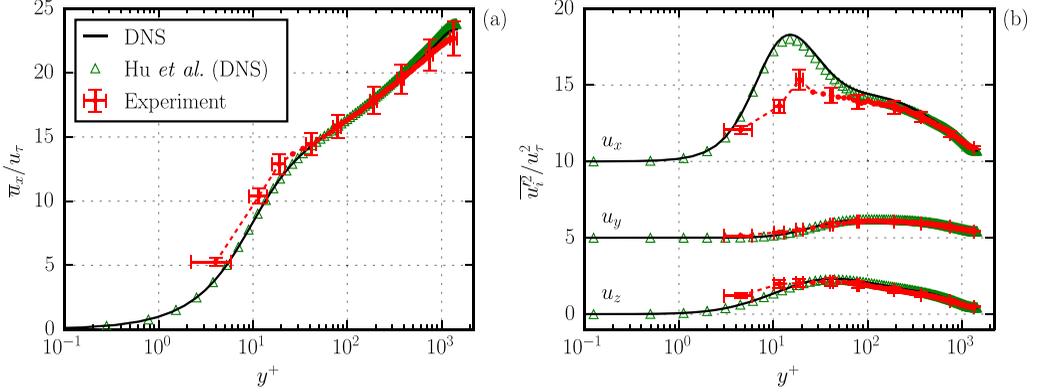
FIG. 3. Mean and variance velocity profiles. Comparison between experiments (dashed lines), DNS (solid lines), and Hu *et al.* [27] DNS at $\mathrm{Re}_\tau = 1440$ (triangles). Velocity variance profiles are shifted vertically for clarity. All quantities are normalized in wall units.

tracers advected by the resolved fluid velocity. The pseudospectral method, described in detail by Buffat *et al.* [24], assumes periodicity in the streamwise (x) and spanwise (z) directions, where a Fourier decomposition of the velocity field is applied. In the wall-normal (y) direction, a Chebyshev expansion is performed in order to enforce no-slip boundary conditions at the walls. The size of the computational domain is $L_x \times L_y \times L_z = 4\pi h \times 2h \times \pi h$ (in wall units, $L_x^+ \times L_y^+ \times L_z^+ = 18166 \times 2891 \times 4541$) in the streamwise, wall-normal, and spanwise directions, respectively. The velocity field is decomposed into $2048 \times 433 \times 1024$ spectral modes. In physical space, this corresponds to a uniform grid spacing $\Delta x^+ = 8.9$ and $\Delta z^+ = 4.4$ in the streamwise and spanwise directions, respectively. In the wall-normal direction, the grid spacing Δy^+ varies between 0.04 (wall region) and 10.5 (channel center). An explicit second-order Adams-Bashforth scheme is used to advance the resolved equations in time, with a simulation time step $\Delta t^+ = 0.03$. The total simulation time in channel units is $TU/h = 217$, which corresponds to about 17 turnover times of the centerline flow.

Once the instantaneous velocity field **u** is known, the acceleration field is computed in the Eulerian frame according to $\mathbf{a} = \partial\mathbf{u}/\partial t + \nabla(\mathbf{u}^2/2) + (\nabla \times \mathbf{u}) \times \mathbf{u}$. Orzag's 2/3 rule [25] is applied in the x and z directions to the velocity and acceleration fields to filter out aliasing noise resulting from evaluation of nonlinear terms.

The simulation is started with a fully developed, statistically stationary turbulent channel flow containing 2×10^6 randomly distributed fluid particles. Velocity and acceleration of fluid particles are determined from interpolation of the respective Eulerian fields at each particle location using third-order Hermite polynomials. The choice of the interpolation scheme is critical, particularly for the evaluation of Lagrangian acceleration statistics. Lower-order schemes such as trilinear or Lagrange interpolation lead to spurious oscillations which are clearly visible in the temporal spectrum of particle acceleration [13,26]. Particle positions are advanced in time using a second-order Adams-Bashforth scheme, as for the Eulerian velocity field. Sample trajectories obtained from this procedure are shown in Figs. 1 and 5.

In Fig. 3 mean and variance velocity profiles from experiments and simulations are compared with the channel flow DNS of Hu *et al.* [27] at roughly the same Reynolds number $\mathrm{Re}_\tau = 1440$. Experimental profiles are obtained by sampling the instantaneous velocity of particles conditioned by their wall distance y^+. In the three cases, the mean streamwise velocity profile presents a clear logarithmic behavior over $40 \lesssim y^+ \lesssim 1200$. Results from both simulations are consistent with each other, while slight departures in the mean profile are observed for the experiments. These differences are more pronounced near the wall ($y^+ < 30$) and towards the channel center ($y^+ > 500$). Similar remarks can be made for the streamwise velocity variance, where an important difference is found at
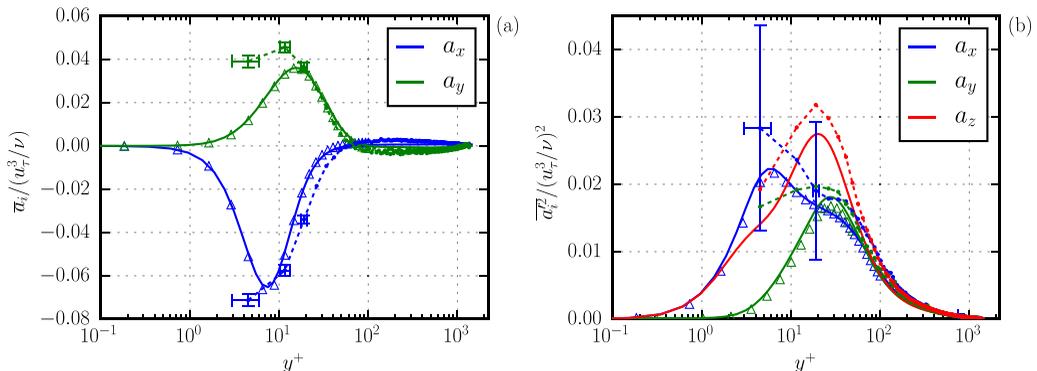
FIG. 4. Mean and variance acceleration profiles. Comparison between experiments (dashed lines), DNS (solid lines), and Yeo *et al.* [30] DNS at $\mathrm{Re}_\tau = 600$ (triangles).

$y^+ < 50$ relative to the simulations. On the other hand, wall-normal and transverse velocity variances from experiments are in agreement with the simulations at all measured wall distances.

Error bars shown on the experimental results in Fig. 3 and the following experimental results reported in this paper (with the exception of the probability density function results discussed in Sec. V) are calculated statistically for a 95% confidence interval [28]. Error bars also take into account the experimental precision associated with the parameters used to report normalized results, u_τ, ν, etc., which is incorporated into the error calculation in the standard way [29] and in some cases is responsible for a large part of the error, as in the plot of $\overline{a'^2}/(u_\tau^3/\nu)^2$ shown in Fig. 4.

Figure 4 shows the mean and variance acceleration profiles obtained by our experiments and DNS. The profiles are consistent with the DNS results of Yeo *et al.* [30] (also presented in the figure) even though their simulations were performed at a considerably lower Reynolds number $\mathrm{Re}_\tau = 600$. As shown by Yeo *et al.* [30], the mean streamwise acceleration can be decomposed into an irrotational and a solenoidal contribution, associated with the mean streamwise pressure gradient and the viscous stress, respectively. In wall units, this is expressed as $\overline{a}_x^+ = \overline{a}_x^{I+} + \overline{a}_x^{S+} = \frac{1}{\mathrm{Re}_\tau} + \frac{d^2\overline{u}_x^+}{dy^{+2}}$. Near the wall, the solenoidal term $\overline{a}_x^S$ dominates and is negative, which shows that the negative peak of mean streamwise acceleration at $y^+ \approx 7$ is a consequence of a viscous contribution. For the mean wall-normal acceleration, the solenoidal term $\overline{a}_y^S$ is zero. Therefore, its profile is entirely determined by the mean wall-normal pressure gradient [30].

Profiles of acceleration variance [Fig. 4(b)] reveal qualitative agreement between both sets of data, although large uncertainty is seen in the experimental results near the wall. It is worth noting that, at their respective peaks, the standard deviation of acceleration is larger than the magnitude of the mean acceleration, indicating that dynamics near the wall are strongly influenced by acceleration fluctuations. As shown by Lee *et al.* [21], these dynamics are dominated by the presence of near-wall streamwise vortices inducing high-magnitude, oscillating centripetal accelerations mainly oriented in the spanwise and wall-normal directions.

III. LAGRANGIAN CORRELATIONS

The Lagrangian description deals with particle trajectories that are parameterized by their initial position $\mathbf{r}_0$ and by the time delay τ relative to the initial time t_0. In stationary HIT, Lagrangian statistics do not depend on $\mathbf{r}_0$ due to translational invariance, nor on t_0 due to statistical stationarity. Statistics are thus parametrized only by the time delay τ. Furthermore, single-point single-time statistics such as moments of acceleration components $\langle a_i^p(\tau) \rangle$ are constant in τ. In inhomogeneous turbulence, things are more complex. Indeed the initial position $\mathbf{r}_0$ must be retained. The symmetries of the channel flow are such that the dependency of the statistics on $\mathbf{r}_0$ reduces to a dependency on the
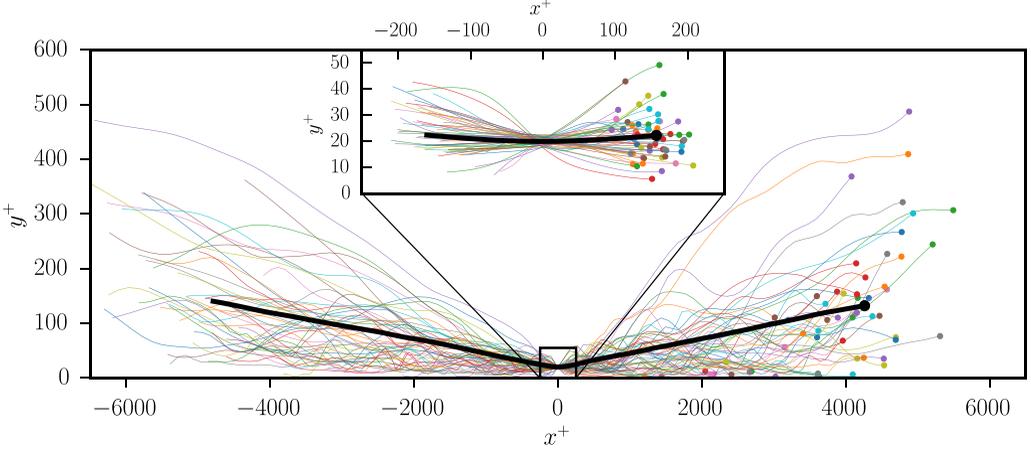
FIG. 5. Illustration of the Lagrangian averaging procedure. Thin curves represent trajectories of particles located at $y^+ = y_0^+ \pm 0.5\,\delta y^+$ at a reference time t_0 (here $y_0^+ = 20$ and $\delta y^+ = 5$). Trajectories are shifted in the streamwise direction so that $x(t_0) = 0$. The thick curve represents the Lagrangian average of particle position $\langle \mathbf{r}(\tau, y_0) \rangle$. The channel center is at $y^+ = 1440$. Trajectories $\mathbf{r}(t_0 + \tau, y_0)$ are shown for time lags $\tau^+ \in [-338, 338]$. The zoomed inset represents time lags $\tau^+ \in [-13.5, 13.5]$.

initial distance from the wall, y_0. Moreover, single-time Lagrangian statistics now vary with the time delay τ. For instance, the Lagrangian average of the streamwise velocity component, $\langle v_x(t_0 + \tau, y_0) \rangle$, depends on τ because particles move away from their initial distance (toward the center on average; see Fig. 5) and thus experience regions of higher average velocity.

In inhomogeneous flows, the Lagrangian and Eulerian averages coincide only for $\tau = 0$. Stationarity of Eulerian statistics implies that Lagrangian statistics depend only on τ and y_0 and not on t_0. Inhomogeneity also implies that Lagrangian statistics for negative values of τ are *a priori* different from those at positive τ. Practically, estimators of Lagrangian statistics are the following. A small interval of width δy around a given initial value of y_0 is chosen. As soon as a trajectory has a value $y(t)$ that belongs to this interval, the initial time t_0 is set. Statistics are then accumulated as a function of τ. This procedure is illustrated in Fig. 5 for the average particle position $\langle \mathbf{r}(\tau, y_0) \rangle$.

An adequate tool to obtain time scales and coupling between components is the Lagrangian correlation coefficient of fluid particle acceleration, defined as

$$\rho_{ij}(\tau, y_0) = \frac{\langle a_i'(t_0, y_0)\, a_j'(t_0 + \tau, y_0) \rangle}{\langle a_i'^2(t_0, y_0) \rangle^{1/2} \langle a_j'^2(t_0 + \tau, y_0) \rangle^{1/2}}, \tag{4}$$

where $a_i'(t_0 + \tau, y_0) = a_i(t_0 + \tau, y_0) - \langle a_i(t_0 + \tau, y_0) \rangle$ is the fluid particle acceleration fluctuation relative to the Lagrangian average, with $i = x, y$, or z. The estimators thus correlate the initial acceleration with that at a time lag τ along the trajectory of fluid particles initially at y_0.

Figures 6 and 7 show various components of the acceleration correlation tensor ρ_{ij} calculated at different initial wall distances y_0^+. Time lags equal to the local Kolmogorov time scale $\tau_\eta(y) = \sqrt{\nu/\epsilon(y)}$ are also represented in the figures, with the local mean turbulent energy dissipation rate estimated from DNS as $\epsilon = \nu \overline{(\partial_j u_i')(\partial_j u_i')}$.

The inhomogeneity of the flow is visible in the fact that the typical decorrelation time varies significantly over the width of the channel. The anisotropy is visible in the fact that the streamwise and wall-normal components display some nonzero correlation (in contrast with HIT), as shown in Fig 7(b). Cross-correlations with the transverse component remain zero due to the statistical symmetry $z \leftrightarrow -z$, as shown in Fig. 7(c).
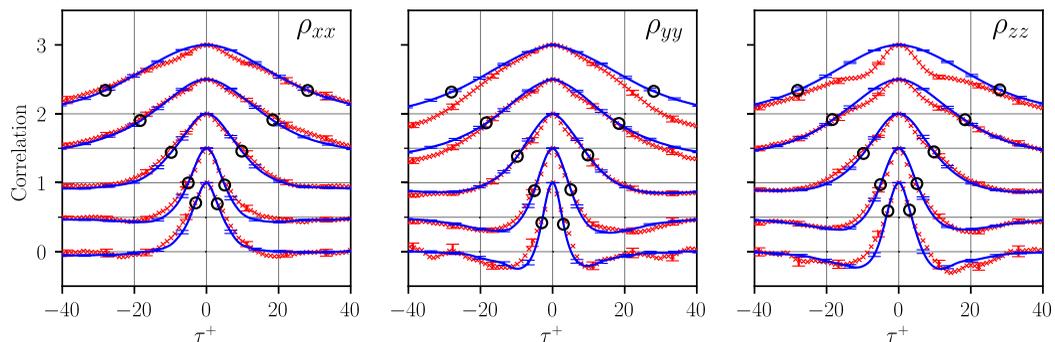
FIG. 6. From left to right, Lagrangian autocorrelations of streamwise (ρ_{xx}), wall-normal (ρ_{yy}), and spanwise (ρ_{zz}) particle acceleration. Experiments, crosses; DNS, lines. Circles indicate time lags $\tau = \pm\tau_\eta$. Curves are shifted vertically by increments of 0.5 for clarity. From bottom to top, the curves correspond to particles located initially at $y_0^+ = 20$, 60, 200, 600, and 1000. Horizontal grid lines show the zero-correlation level for each y_0^+. In the experiment, $\tau^+ = 1$ corresponds to 0.175 ms.

In the vicinity of the wall the decorrelation time is close to one in wall units, showing that this is the adequate characteristic time for rescaling of small-scale quantities such as the acceleration in this region. This will be discussed further in the analysis of the characteristic Lagrangian time scales. A very good agreement is observed between experimental and DNS results, with the exception of the long time behavior of ρ_{yy} at $y^+ = 1000$, and the short time behavior of ρ_{zz} at $y^+ = 1000$. While the former remains unexplained, the latter is due to the higher level of noise in the measurement of the z-component, which is a technical consequence of the way the PTV is performed. Namely, near the center of the channel, the signal-to-noise ratio for the z component of acceleration comes close to the limits of the data processing methods described in Sec. II and in previous work [23], and the correlation of noise is seen in the short time behavior of ρ_{zz} at $y^+ = 1000$.

Previous studies in HIT [31,32] have associated fluid particle acceleration and vortex dynamics by observing that high-acceleration events often correspond to centripetal accelerations in vortex filaments, and the autocorrelation of the centripetal component of these accelerations becomes negative to a much greater degree than the autocorrelation of the component of the acceleration parallel to the vortex filament. Contrary to HIT where there are no preferential directions, in the near-wall region of a wall-bounded turbulent flow the preferential orientation of vortices in the streamwise direction is expected. As shown in Fig. 6, near the wall the autocorrelations of a_y and a_z become negative at approximately $\tau = 2\tau_\eta$ (similarly to the case of HIT), while the correlation
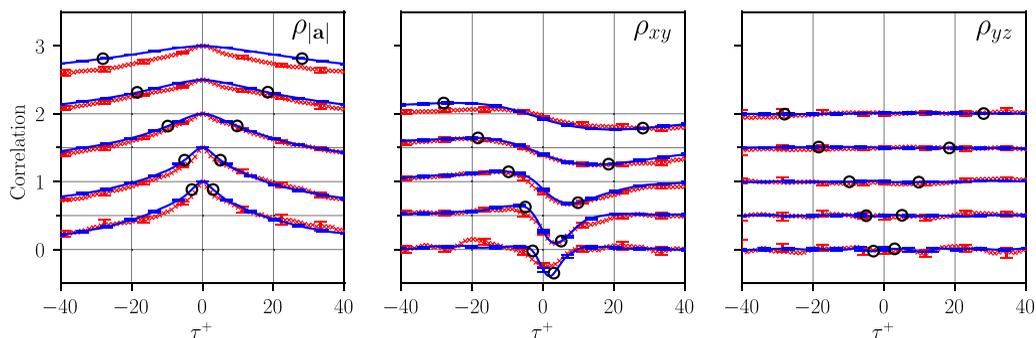

FIG. 7. From left to right, Lagrangian autocorrelation of acceleration magnitude ($\rho_{|\mathbf{a}|}$) and acceleration cross-correlations ρ_{xy} and ρ_{yz}. From bottom to top, the curves correspond to particles located initially at $y_0^+ = 20$, 60, 200, 600, and 1000. (For details, see Fig. 6.)
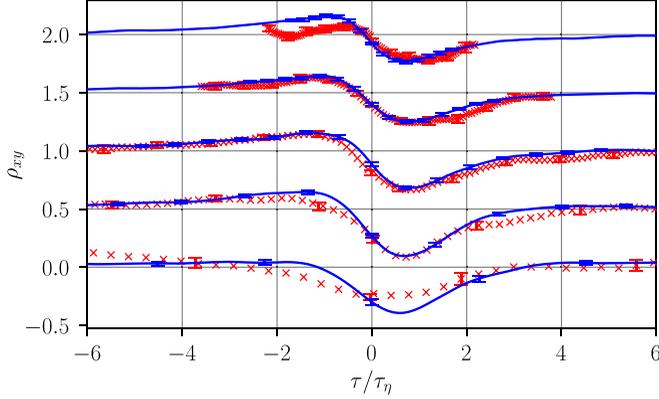
FIG. 8. Lagrangian correlation between streamwise and wall-normal acceleration components. Time delay τ is normalized with the local Kolmogorov time scale τ_η. From bottom to top, the curves correspond to particles located initially at $y_0^+ = 20, 60, 200, 600,$ and 1000. (For details, see Fig. 6.)

of a_x remains positive with a significantly longer initial decorrelation time. The negative ρ_{yy} and ρ_{zz} correlations can be associated with the effect of near-wall streamwise vortices. A fluid particle trapped in one such vortex experiences strong centripetal accelerations towards the vortex rotation axis [21]. This strong form of anisotropy of the acceleration is observed only near the walls ($y^+ < 50$) and becomes negligible towards the channel center, as confirmed below by the acceleration time scales associated to these correlations.

The autocorrelations ρ_{xx} and ρ_{yy} are almost symmetric in time, e.g., $\rho_{xx}(-\tau, y_0) \approx \rho_{xx}(\tau, y_0)$. This symmetry can be explained by the nearly time-symmetric average trajectories in the near-wall region as illustrated in Fig. 5, i.e., $\langle \mathbf{r}(\tau, y_0) \rangle \approx \langle \mathbf{r}(-\tau, y_0) \rangle$. In contrast, the cross-correlation ρ_{xy} is strongly time-asymmetric close to the wall. This asymmetry, along with the nonzero time lag at which the peak is observed suggests the idea of causality between acceleration components. That is, a streamwise acceleration fluctuation is followed on average by an opposite-sign wall-normal acceleration fluctuation. Towards the channel center, this effect persists and the correlation becomes antisymmetric with time, $\rho_{xy}(-\tau) \approx -\rho_{xy}(\tau)$, due to the decreasing influence of wall confinement.

The correlation between a_x and a_y [Fig. 7(b)] is most important near the walls. In that region, the zero-time cross-correlation (equivalent to an Eulerian single-point single-time correlation) is negative due to increased viscous effects combined with confinement by the wall (see the joint PDFs in Sec. V for more details). Moreover, the cross-correlation peak is always found at a nonzero time lag. Far from the wall, the correlation is close to zero at $\tau^+ = 0$, while it increases in absolute value for nonzero time lags. The influence of the boundary layer remains visible even in the bulk of the channel where the correlation is still nonzero, indicating that small-scale anisotropy is still present in that region. In Fig. 8 the ρ_{xy} cross-correlation is displayed as function of the normalized time lag τ/τ_η. The time lag of the negative correlation peak is shown to scale with τ_η, with a value τ/τ_η fluctuating between 0.5 and 0.7 with the wall distance y_0^+.

The $\rho_{xy}(\tau, y_0)$ correlation describes the changes of orientation of the acceleration fluctuation vector $\mathbf{a}'(t_0 + \tau, y_0)$ projected on the x-y plane. Its behavior implies that there is a preferential direction of rotation of $\mathbf{a}'$ along a particle trajectory. Moreover, such changes of orientation happen over times of the order of the Kolmogorov time scale. Thus, this anisotropy is associated with the smallest scales of turbulence and is observed for all wall distances. The preferential direction of rotation implied by the cross-correlation is consistent with the direction of mean shear, represented by an average vorticity $\overline{\omega}_z = -d\bar{u}/dy$ which is negative in the lower half of the channel, where the presented statistics are obtained. This result is consistent with evidence of small-scale anisotropy found in other turbulent flows governed by large-scale anisotropy. For instance, from DNS of

homogeneous shear flow, Pumir and Shraiman [33] found signs of small-scale anisotropy which did not decrease at increasing Reynolds number, in contradiction with Kolmogorov's local isotropy hypothesis [34]. In their work, small-scale anisotropy was quantified by the skewness of the spanwise vorticity ω_z, which was shown to be of the same sign as the large-scale average vorticity. More recently, and using a similar approach, Pumir *et al.* [35] showed the presence of small-scale anisotropy from DNS of turbulent channel flow at $\mathrm{Re}_\tau \approx 1000$ all along the log layer. Our results show that such small-scale anisotropy is also observed by the Lagrangian acceleration statistics. Therefore, a stochastic model for the Lagrangian acceleration which includes elements derived from the ρ_{xy} correlation would be able to reproduce the presence of small-scale anisotropy in shear flows.

In Fig. 7(a) we plot the autocorrelation of the acceleration magnitude $|\mathbf{a}|$, showing that this quantity stays correlated for far longer than each acceleration component. This behavior is observed at all wall distances and is consistent with results in HIT [36,37]. It is explained by the fact that changes in the orientation of the acceleration vector are much more sudden than changes in its magnitude. In near-wall turbulence, this observation is again explained by centripetal acceleration induced by streamwise vortices, which preserve the acceleration magnitude for a longer time than the acceleration orientation [21].

IV. LAGRANGIAN TIME SCALES

The characteristic time scale associated to each acceleration component is estimated according to

$$T_{a,i}(y_0) = \int_0^{\tau_c} \rho_{ii}(\tau, y_0)\, d\tau, \tag{5}$$

where τ_c is the time lag at which the autocorrelation first crosses 0.05. This definition is chosen because the classical definition with the integration going to infinite time cannot be applied to all acceleration components since some correlations become negative. This is also the case for HIT for which the integral of the acceleration correlations is actually zero because of the stationarity of the velocity. The usual zero-crossing time as in Yeung and Pope [36] can neither be used here because some correlations (near the center of the channel) do not cross zero during the observation time. Our definition is a convenient mix between these two usual definitions of the typical time scale.

Lagrangian velocity (integral) time scales $T_{v,i}$, as well as the acceleration norm time scale $T_{|\mathbf{a}|}$, are defined equivalently. Due to the limited measurement volume in the experiment, the full decorrelation of the autocorrelations of velocity and the norm of the acceleration is not achieved at all wall distances in the channel. These autocorrelations have been extrapolated as illustrated by Fig. 9, and the uncertainty of these results increases with increased extrapolation. This extrapolation is not necessary for the acceleration autocorrelations shown in Fig. 6 (which decay much faster) and thus for the computation of the time scales $T_{a,i}$.

The evolution of all time scales with wall distance is shown in Fig. 10. As can be deduced from the autocorrelation curves, the acceleration time scales $T_{a,i}$ and $T_{|\mathbf{a}|}$ generally increase with wall distance. The same is observed for the Lagrangian velocity time scales. The acceleration norm time scale $T_{|\mathbf{a}|}$ is about one order of magnitude larger than the time scale of the acceleration components. It is of the order of the integral time scales $T_{v,i}$.

In Fig. 11 the Lagrangian acceleration time scales are normalized with the local Kolmogorov time scale. Both ϵ and τ_η vary with wall distance. The acceleration time scales are of the order of τ_η all along the channel. The normalized time scales only weakly change for $y^+ > 80$, reaching a value between 0.8 and 0.9 in the bulk of the channel. However, in that region, small differences persist between $T_{a,y}$ and the time scales obtained for the other two components, suggesting once more that anisotropy is still present far from the wall. Close to the wall ($y^+ \lesssim 40$), the longer correlation time of the streamwise acceleration is reflected in a larger time scale $T_{a,x}$ compared to the other components.
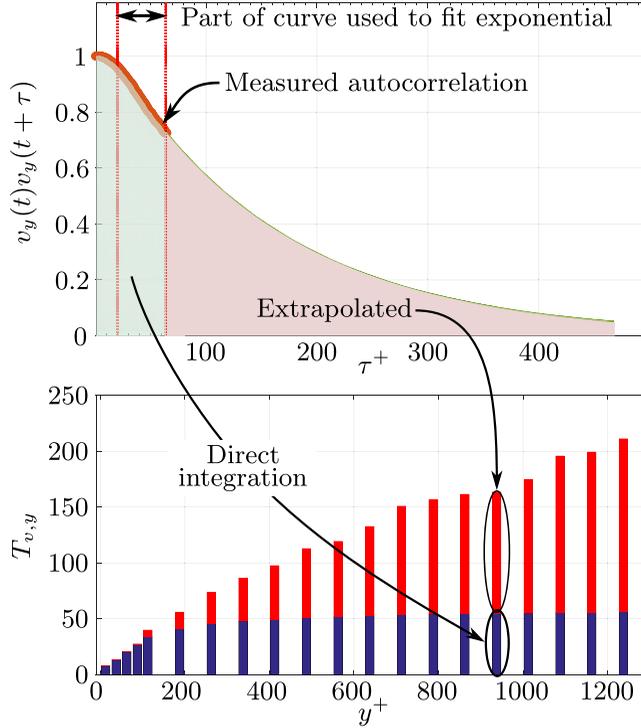
FIG. 9. An example of how Lagrangian velocity time scales are calculated. The autocorrelation of the wall-normal component of velocity from $y^+ = 925$ is shown (top plot) in red, where the part of the measured autocorrelation used to fit the exponential extrapolation is also shown. The bottom plot shows the Lagrangian wall-normal velocity time scale across the channel, where the portion of the time scale that is directly measured is shown in blue and the portion of the time scale that comes from the extrapolation is shown in red.

Figure 12(a) shows the ratio of Lagrangian time scales of velocity and acceleration for each component. Also shown in Fig. 12(a) is Eq. (3), the empirical fit to the DNS data of Yeung and Pope [36] proposed by Sawford [6], using the profile of Re_λ calculated from the DNS and $C_0 = 7$ as suggested by Sawford. The HIT model follows the trend of the data. However, there is significant
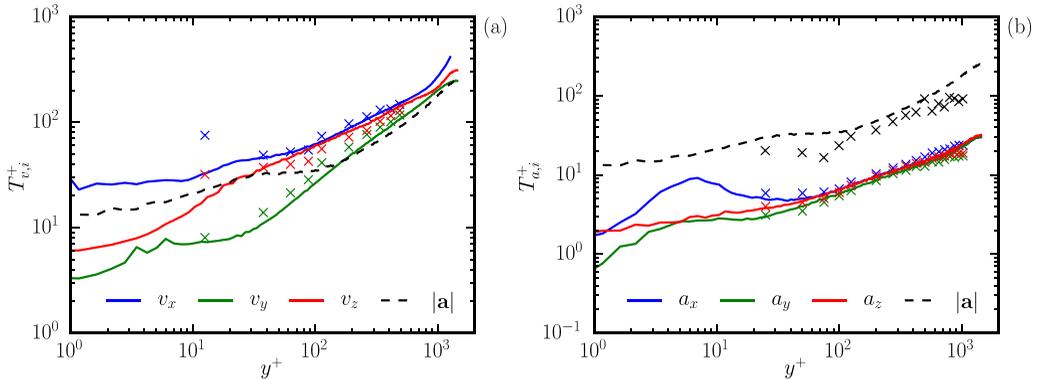

FIG. 10. Lagrangian velocity and acceleration time scales in wall units. Experiments, crosses; DNS, solid lines. The acceleration magnitude time scale $T_{|\mathbf{a}|}$ is represented by dashed lines.
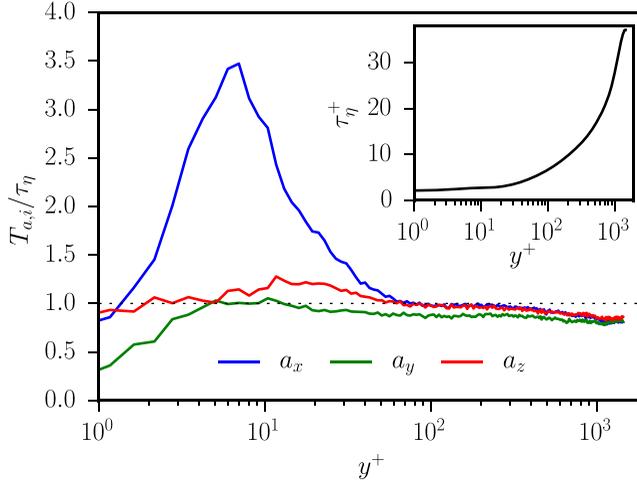
FIG. 11. Lagrangian acceleration time scales normalized by the local Kolmogorov time scale (DNS results only). Inset: local Kolmogorov time scale in wall units.

anisotropy in these ratios of time scales that extends far away from the wall. First-order Lagrangian stochastic models in velocity such as given by Eq. (1) are based implicitly on the scale separation between the velocity and the acceleration time scales. Here a small separation is seen between these two time scales near the wall. Significantly, the time scale ratio for the wall-normal component (*y*) is approximately half of that predicted by the local Reynolds number (the HIT model plotted in the figure) near the wall. Even farther from the wall, this time scale ratio is significantly overpredicted by the HIT model.

The long time scales of the acceleration norm previously reported have inspired the development of a Lagrangian subgrid stochastic model that models the acceleration norm and acceleration direction as two independent stochastic processes [3,38]. Figure 12(b) shows that the ratios of Lagrangian time scales of acceleration norm to acceleration components are only weakly varying for $y^+ > 50$ and comparable in magnitude to the ratios of Lagrangian velocity and acceleration time scales.
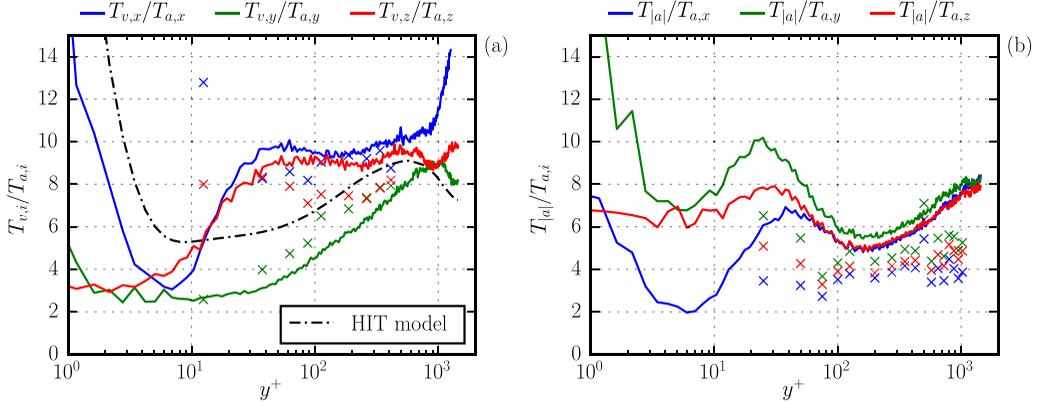

FIG. 12. Lagrangian time scale ratios. Experiments, crosses; DNS, solid lines. (a) Ratio between the Lagrangian velocity and acceleration time scales, by component. Also shown is the HIT model [6] for the ratio of Lagrangian velocity and acceleration time scales. (b) Ratio between the time scales of acceleration magnitude and the components of acceleration.
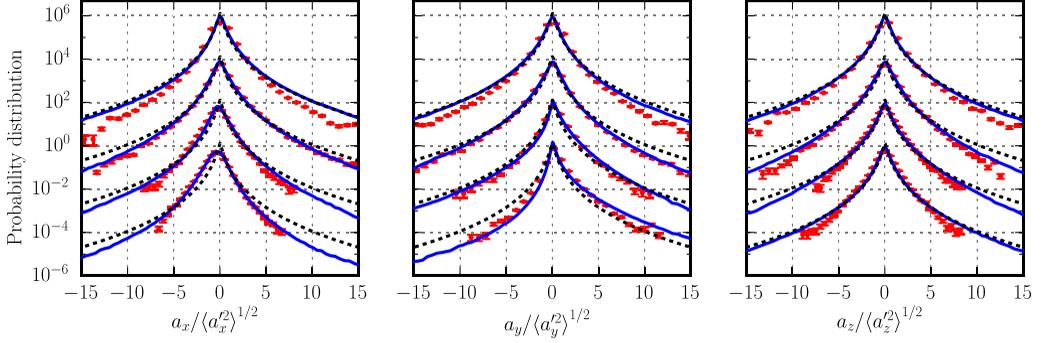
FIG. 13. PDF of streamwise, wall-normal, and spanwise particle acceleration. Experiments, symbols with error bars; DNS, lines. The dashed lines represent the theoretical prediction for the acceleration PDF in HIT [37]. The PDFs are normalized by the root-mean-square value of acceleration. From bottom to top, the curves correspond to particles located at $y^+ = 10, 20, 200$, and 1200. The statistical convergence of the experimental data is shown by error bars proportional to $1/\sqrt{n_i}$ where n_i is the number of events in bin i.

V. DISTRIBUTIONS

Figure 13 shows the probability distribution function (PDF) of the three acceleration components obtained at different wall distances. All curves present very long tails corresponding to extremely high-acceleration events associated to intermittency [8]. Once again, good agreement is achieved between the experiments and the DNS. The acceleration PDFs are also compared with the functional shape proposed by Mordant *et al.* [37] for HIT, which assumes that the acceleration magnitude follows a log-normal probability distribution and that the acceleration vector is isotropic. According to those assumptions, the PDF of an acceleration component is given by

$$P(a_i) = \frac{e^{s^2/2}}{4m}\left[1 - \text{erf}\left(\frac{\ln\frac{|a_i|}{m} + s^2}{\sqrt{2}s}\right)\right],\tag{6}$$
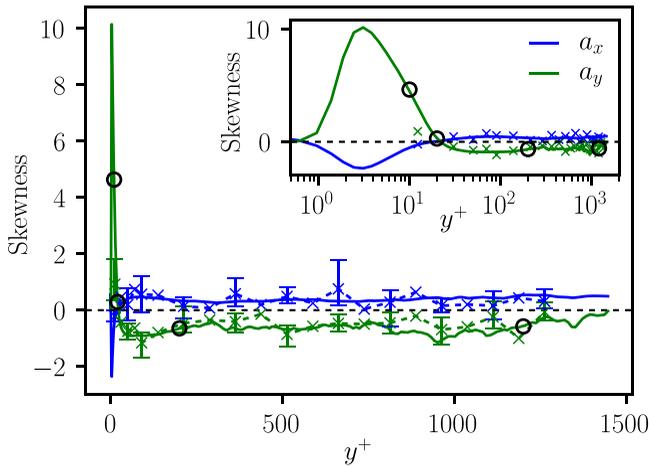

FIG. 14. Skewness of streamwise and wall-normal acceleration components. Experiments, crosses; DNS, lines. Circles indicate skewness of a_y at $y^+ = 10, 20, 200$, and 1200. Inset: skewness profiles with y^+ in logarithmic scale.
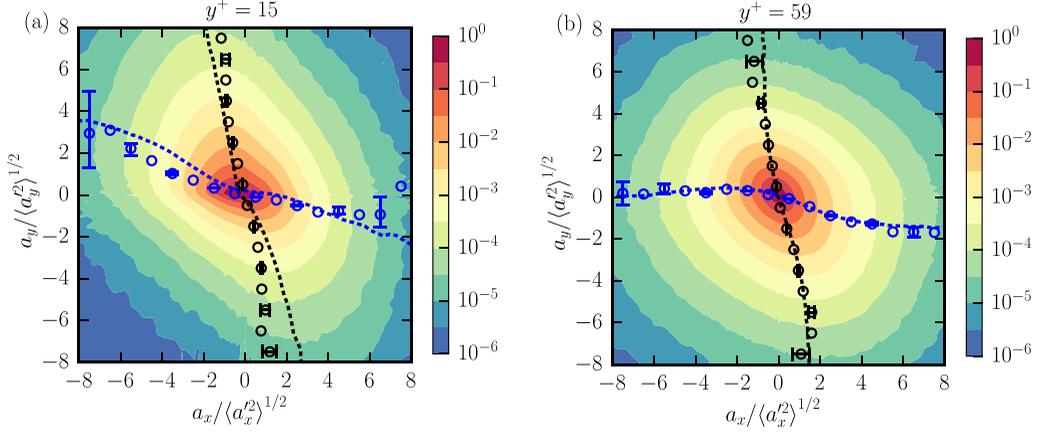
FIG. 15. Joint PDF of streamwise and wall-normal acceleration at $y^+ = 15$ and 59. Conditional means $\langle a_x|a_y \rangle/\langle a_x'^2 \rangle^{1/2}$ and $\langle a_y|a_x \rangle/\langle a_y'^2 \rangle^{1/2}$ are superposed to the contours using black and blue markers, respectively. Experiments, circles; DNS, dashed lines.

where m determines the variance of a_i ($m = \sqrt{3/e^{2s^2}}$ for variance 1), while s determines the shape of the PDF. A value $s = 1$ is used in the comparisons. Towards the channel center, the PDFs of the three acceleration components match this prediction, suggesting that the instantaneous behavior of acceleration becomes close to isotropic. More strikingly, the spanwise acceleration seems to match the prediction very close to the wall, suggesting that this component is not affected by anisotropy as in the other two directions. The general agreement with the shape of the HIT PDF suggests that intermittency is extremely strong in the boundary layer although the Reynolds number is moderate: $Re_\lambda \sim 60$ to 100 in our flow whereas it was close to 1000 in Mordant *et al.* [37]. It implies also that this shape of the PDF presents some universality.

The PDFs of the streamwise and wall-normal acceleration components become quite asymmetric near the wall. This asymmetry is quantified by their skewness $S_i = \langle a_i'^3 \rangle/\langle a_i'^2 \rangle^{3/2}$ shown in Fig. 14. Due to flow symmetry, the skewness of a_z is zero. Very close to the wall, S_x and S_y are strongly negative and positive, respectively, indicating that their PDFs are very asymmetric due to wall-induced anisotropy. The signs of S_x and S_y are both inverted after $y^+ \approx 20$. Their respective values remain different from zero and change little for $y^+ > 80$. This reinforces the idea that turbulence anisotropy is still present in the channel center.

The dependency between the acceleration components is analyzed by the joint PDF, $P(a_x, a_y)$. Figure 15 shows the results obtained at two wall distances, $y^+ = 15$ and 59. Close to the wall [Fig. 15(a)], the joint PDF has a stretched shape, showing a preference for events given by $a_x < 0$ and $a_y > 0$. These events can be associated to fluid particles advected towards the wall. These particles move towards regions of decreasing mean streamwise velocity, leading on average to a streamwise deceleration of their motion ($a_x < 0$). Simultaneously, their negative wall-normal velocity goes to zero due to confinement by the wall, resulting in a positive wall-normal acceleration ($a_y > 0$). This dependency between both acceleration components is confirmed by the conditional means $\langle a_x|a_y \rangle$ and $\langle a_y|a_x \rangle$, which are superposed to the joint PDF contours. Particles advected away from the wall are less affected by wall confinement, and thus the impact on their wall-normal acceleration is less visible in the joint PDF. Nonetheless, on average, those particles also experience the effect of the mean velocity gradient, which results in this case in a positive streamwise acceleration.

VI. CONCLUDING REMARKS

By performing both DNS and experiments, the highly anisotropic turbulent flow in the vicinity of channel walls is described in terms of Lagrangian statistics. Near-wall vortical structures are

clearly identified by their influence on the acceleration autocorrelations. Viscous effects and wall-confinement have also a strong impact on acceleration statistics as evidenced by the joint PDFs. Less expectedly, signs of small-scale anisotropy are present across the channel. The observed behavior of the Lagrangian time scales can be a basis for the formulation of Lagrangian stochastic models of acceleration applied to wall-bounded turbulent flows. These models must also take into account the dependency among acceleration components, which is apparent in the presented cross-correlations and joint PDFs of acceleration. Acceleration models based on the presented results should be able to capture the effects of (1) the near-wall dynamics associated with confinement and coherent structures and (2) the small-scale anisotropy present in the whole channel.

[1] P. Sagaut, *Large Eddy Simulation for Incompressible Flows: An Introduction*, 3rd ed. (Springer, Berlin, 2006).

[2] S. B. Pope, PDF methods for turbulent reactive flows, Prog. Energy Combust. Sci. **11**, 119 (1985).

[3] R. Zamansky, I. Vinkovic, and M. Gorokhovski, Acceleration in turbulent channel flow: Universalities in statistics, subgrid stochastic models and an application, J. Fluid Mech. **721**, 627 (2013).

[4] S. B. Pope, Lagrangian PDF methods for turbulent flows, Ann. Rev. Fluid Mech. **26**, 23 (1994).

[5] G. I. Taylor, Diffusion by continuous movements, Proc Lond. Math. Soc. **s2-20**, 196 (1922).

[6] B. L. Sawford, Reynolds number effects in Lagrangian stochastic models of turbulent dispersion, Phys. Fluids A **3**, 1577 (1991).

[7] S. B. Pope, Stochastic Lagrangian models of velocity in homogeneous turbulent shear flow, Phys. Fluids **14**, 1696 (2002).

[8] A. La Porta, G. A. Voth, A. M. Crawford, J. Alexander, and E. Bodenschatz, Fluid particle accelerations in fully developed turbulence, Nature (London) **409**, 1017 (2001).

[9] S. B. Pope and Y. L. Chen, The velocity-dissipation probability density function model for turbulent flows, Phys. Fluids A **2**, 1437 (1990).

[10] C. Beck, Dynamical Foundations of Nonextensive Statistical Mechanics, Phys. Rev. Lett. **87**, 180601 (2001).

[11] A. M. Reynolds, On the application of nonextensive statistics to Lagrangian turbulence, Phys. Fluids **15**, L1 (2003).

[12] N. Mordant, J. Delour, E. Lévêque, A. Arnéodo, and J.-F. Pinton, Long Time Correlations in Lagrangian Dynamics: A Key to Intermittency in Turbulence, Phys. Rev. Lett. **89**, 254502 (2002).

[13] J.-I. Choi, K. Yeo, and C. Lee, Lagrangian statistics in turbulent channel flow, Phys. Fluids **16**, 779 (2004).

[14] L. Chen, S. W. Coleman, J. C. Vassilicos, and Z. Hu, Acceleration in turbulent channel flow, J. Turbulence **11**, N41 (2010).

[15] R. J. E. Walpot, C. W. M. van der Geld, and J. G. M. Kuerten, Determination of the coefficients of Langevin models for inhomogeneous turbulent flows by three-dimensional particle tracking velocimetry and direct numerical simulation, Phys. Fluids **19**, 045102 (2007).

[16] L. Del Castello and H. J. H. Clercx, Lagrangian Acceleration of Passive Tracers in Statistically Steady Rotating Turbulence, Phys. Rev. Lett. **107**, 214502 (2011).

[17] S. Gerashchenko, N. S. Sharp, S. Neuscamman, and Z. Warhaft, Lagrangian measurements of inertial particle accelerations in a turbulent boundary layer, J. Fluid Mech. **617**, 255 (2008).

[18] A. Taniére, B. Arcen, B. Oesterlé, and J. Pozorski, Study on Langevin model parameters of velocity in turbulent shear flows, Phys. Fluids **22**, 115101 (2010).

[19] J. G. M. Kuerten and J. J. H. Brouwers, Lagrangian statistics of turbulent channel flow at $Re_\tau = 950$ calculated with direct numerical simulation and Langevin models, Phys. Fluids **25**, 105108 (2013).

[20] A. J. Smits, B. J. McKeon, and I. Marusic, High Reynolds number wall turbulence, Annu. Rev. Fluid Mech. **43**, 353 (2011).

[21] C. Lee, K. Yeo, and J.-I. Choi, Intermittent Nature of Acceleration in Near Wall Turbulence, Phys. Rev. Lett. **92**, 144502 (2004).

[22] N. T. Ouellette, H. Xu, and E. Bodenschatz, A quantitative study of three-dimensional Lagrangian particle tracking algorithms, Exp. Fluids **40**, 301 (2006).

[23] N. Mordant, A. M. Crawford, and E. Bodenschatz, Experimental Lagrangian acceleration probability density function measurement, Physica D **193**, 245 (2004).

[24] M. Buffat, L. Le Penven, and A. Cadiou, An efficient spectral method based on an orthogonal decomposition of the velocity for transition analysis in wall bounded flow, Comput. Fluids **42**, 62 (2011).

[25] S. A. Orszag, On the elimination of aliasing in finite-difference schemes by filtering high-wavenumber components, J. Atmos. Sci. **28**, 1074 (1971).

[26] M. A. T. van Hinsberg, J. H. M. ten Thije Boonkkamp, F. Toschi, and H. J. H. Clercx, Optimal interpolation schemes for particle tracking in turbulence, Phys. Rev. E **87**, 043307 (2013).

[27] Z. Hu, C. L. Morfey, and N. D. Sandham, Wall pressure and shear stress spectra from direct simulations of channel flow, AIAA J. **44**, 1541 (2006).

[28] L. H. Benedict and R. D. Gould, Towards better uncertainty estimates for turbulence statistics, Exp. Fluids **22**, 129 (1996).

[29] R. J. Moffat, Describing the uncertainties in experimental results, Exp. Therm Fluid Sci. **1**, 3 (1988).

[30] K. Yeo, B.-G. Kim, and C. Lee, On the near-wall characteristics of acceleration in turbulence, J. Fluid Mech. **659**, 405 (2010).

[31] N. Mordant, E. Lévêque, and J.-F. Pinton, Experimental and numerical study of the Lagrangian dynamics of high Reynolds turbulence, New J. Phys. **6**, 116 (2004).

[32] F. Toschi, L. Biferale, G. Boffetta, A. Celani, B. J. Devenish, and A. Lanotte, Acceleration and vortex filaments in turbulence, J. Turbulence **6**, N15 (2005).

[33] A. Pumir and B. I. Shraiman, Persistent Small Scale Anisotropy in Homogeneous Shear Flows, Phys. Rev. Lett. **75**, 3114 (1995).

[34] A. N. Kolmogorov, The local structure of turbulence in incompressible viscous fluid for very large Reynolds numbers, Dokl. Akad. Nauk SSSR **30**, 301 (1941).

[35] A. Pumir, H. Xu, and E. D. Siggia, Small-scale anisotropy in turbulent boundary layers, J. Fluid Mech. **804**, 5 (2016).

[36] P. K. Yeung and S. B. Pope, Lagrangian statistics from direct numerical simulations of isotropic turbulence, J. Fluid Mech. **207**, 531 (1989).

[37] N. Mordant, A. M. Crawford, and E. Bodenschatz, Three-Dimensional Structure of the Lagrangian Acceleration in Turbulent Flows, Phys. Rev. Lett. **93**, 214501 (2004).

[38] V. Sabel'nikov, A. Chtab-Desportes, and M. Gorokhovski, New sub-grid stochastic acceleration model in LES of high-Reynolds-number flows, Eur. Phys. J. B **80**, 177 (2011).